Scalar statistics in variable property turbulent channel flows

Ashish Patel,[*] Bendiks J. Boersma, and Rene Pecnik[†]

Process and Energy Department, Delft University of Technology, Leeghwaterstraat 39,
2628 CB Delft, The Netherlands

Direct numerical simulation of fully developed, internally heated channel flows with isothermal walls is performed using the low-Mach-number approximation of Navier-Stokes equation to investigate the influence of temperature-dependent properties on turbulent scalar statistics. Different constitutive relations for density ρ, viscosity μ, and thermal conductivity λ as a function of temperature are prescribed in order to characterize the turbulent scalar statistics. It is shown that the dominant effect caused by property variations on scalar statistics can be parameterized by two nondimensional parameters, namely the semilocal Reynolds number $\mathrm{Re}_\tau^\star \equiv \mathrm{Re}_\tau \sqrt{(\overline{\rho}/\rho_w)}/(\overline{\mu}/\mu_w)$ (the bar and subscript w denote Reynolds averaging and wall value respectively, while Re_τ is the friction Reynolds number based on wall values), and the local Prandtl number $\mathrm{Pr}^\star = \mathrm{Pr}_w(\overline{\mu}/\mu_w)/(\overline{\lambda}/\lambda_w)$ (Pr_w is the molecular Prandtl number based on wall values). Near-wall gradients in $\mathrm{Re}_\tau^\star$ modulate the turbulent heat flux generation mechanism because of structural changes in turbulence. However, the influence of these modulations on the inner scaling of turbulent heat conductivity normalized by local mean viscosity is shown to be weak. Using this observation, a temperature transformation is derived that is invariant of $\mathrm{Re}_\tau^\star$ variations and only exhibits a $\mathrm{Pr}^\star$-dependent shift.

I. INTRODUCTION

Wall-bounded turbulence involving mixing of scalars, such as temperature or concentration fields, plays an important role in many engineering applications. In applications with small variations in temperature or concentration, the scalar field is passive, as they do not influence the turbulent motions. A significant amount of studies involving direct numerical simulation (DNS) of turbulent passive scalar transport have been performed at different Reynolds and Prandtl numbers (or Schmidt number, if the scalar is a concentration field) during the past few decades. One of the important aspects in all these studies involve investigating the analogy between momentum transfer and scalar transport, since it results in a simple modeling approach, where the turbulent scalar flux is determined by the turbulent eddy viscosity μ_t and a turbulent Prandtl (or Schmidt) number Pr (or Sc_t), which is defined as the ratio of eddy viscosity μ_t to eddy conductivity α_t. Kim and Moin [1] and Kawamura *et al.* [2] performed DNS of turbulent heat transfer in a channel at a friction Reynolds number of $\mathrm{Re}_\tau = 180$ and Prandtl numbers Pr_w ranging from 0.1 to 2 in the former study and 0.025 to 5 in the latter. For fluids with $\mathrm{Pr}_w > 0.1$, the turbulent Prandtl number was found to be independent of Pr_w, with values of the order of unity in the regions away from the center. Schwertfirm and Manhart [3] performed DNS with Schmidt number Sc_w up to 50 and found that near the wall Sc_t increases for higher Sc_w. Kawamura *et al.* [4] studied the effect of varying Re_τ (=180, 395) and Pr_w (=0.025, 0.2, 0.71) in a channel and found that Pr_t is independent of Re_τ and Pr_w, if $\mathrm{Pr}_w > 0.2$. Pirozzoli *et al.* [5] extended DNS of passive scalars in channel flows to $\mathrm{Re}_\tau \approx 4000$, with $\mathrm{Pr}_w = 0.2, 0.71, 1$. The turbulent Prandtl number was found to be nearly constant in the lower 50% of the half-channel, regardless of the Reynolds and Prandtl number. The slope of the log-law for the mean scalar profile, which also is directly related to the turbulent Prandtl number, was found to be 1/0.46.

[*]a.patel@tudelft.nl
[†]r.pecnik@tudelft.nl

ASHISH PATEL, BENDIKS J. BOERSMA, AND RENE PECNIK

In applications with large temperature or concentration differences, the variation of scalar dependent thermophysical properties can be strong. Some of the well-known examples which involve variable thermophysical properties include supersonic flows for aircraft and propulsion systems, strongly heated or cooled flows in heat exchangers, or chemically reacting flows in combustion chambers. Furthermore, recently, in order to increase the efficiency of power cycles, there is increased interest in studying turbulent heat transfer to fluids at supercritical pressure [6–8]. These fluids exhibit strong thermophysical property variations due to a strong dependence of properties on temperature. In all such cases, the effects of thermophysical property variations can be strong enough to modulate turbulence and the traditional approach of treating temperature as a passive scalar no longer holds. Although turbulence modulation in a turbulent channel flow due to variable thermophysical properties has been investigated in great detail in high-Mach-number flows [9–12] and in low-Mach-number flows [13–16], the effect of property variations on scalar transport is not well understood. Lee *et al.* [17] studied the influence of wall heating on turbulent thermal boundary layers with variable viscosity and observed variations in mean scalar, scalar fluctuation, and scalar flux, relative to a reference isothermal flow. In order to account for an inhomogeneous Prandtl number distribution, they proposed to modify Kader's relation [18] for the mean scalar profile by incorporating both the local Prandtl number and the Prandtl number at the the inner edge of the log-layer. Nemati *et al.* [19] studied the effect of thermal boundary conditions on developing turbulent pipe flows with fluids at supercritical pressure. Two different thermal wall boundary conditions were studied: The first corresponds to a Neumann boundary condition that permits wall temperature fluctuations and the second corresponds to a Dirichlet boundary condition that does not allow wall temperature fluctuations. They showed that the mean enthalpy and Nusslet number are significantly affected because of wall thermal fluctuations, a result which is in contrast to constant property cases which are known to be independent of wall thermal fluctuation for Prandtl numbers above unity [20–22].

In our previous work [15], we provided a theoretical framework for the semilocal scaling that has been proposed based on heuristic arguments by Huang *et al.* [23]. In contrast to the conventional scaling with wall values, the semilocal scaling uses the wall-shear stress τ_w and the mean local properties to define the characteristic friction velocity and viscous length scale as $u_\tau^\star = \sqrt{\tau_w/\overline{\rho}}$ and $\delta_v^\star = \overline{\mu}/\overline{\rho} u_\tau^\star$, respectively (bar denotes Reynolds averaging). This leads to the semilocally scaled wall distance $y^\star = y/\delta_v^\star$ and the corresponding semilocal Reynolds number $\mathrm{Re}_\tau^\star = h/\delta_v^\star = \mathrm{Re}_\tau \sqrt{(\overline{\rho}/\rho_w)}/(\overline{\mu}/\mu_w)$ (h is the half-channel height or boundary layer thickness and subscript w denotes averaged wall value). The theoretical framework involved a scaling transformation to the Navier-Stokes equations, which is based on local mean values of density $\overline{\rho}$, viscosity $\overline{\mu}$, and semilocal friction velocity $u_\tau^\star = \sqrt{\tau_w/\overline{\rho}}$. The framework further suggests that leading-order effects of property variations on turbulence can effectively be characterized by the semilocal Reynolds number. In order to test the framework and to further investigate the turbulence statistics, a DNS database was generated by solving the low-Mach-number approximation of Navier-Stokes equation in a fully developed internally heated channel flow. Further analysis of the scaling characteristics of turbulent velocity statistics and of turbulence structures were performed by Patel *et al.* [16]. It was shown that the semilocal Reynolds number accommodates the change in viscous scales due to property variations and also provides a measure of near-wall turbulence modulation with respect to a constant property case. For example, cases with decreasing $\mathrm{Re}_\tau^\star$ away from the wall show an increased streamwise anisotropy in the near-wall region, which alters the Reynolds-stress-generation mechanism and modifies the near-wall universality of turbulence. The structural change, however, does not significantly affect the universality of the viscous shear stress as a function of the semilocal wall coordinate. This observation was then used to derive an extension of van Driest velocity transformation defined as $\overline{u}^\star = \int_0^{\overline{u}^{\mathrm{vD}}} (1 + (y/\mathrm{Re}_\tau^\star)d\mathrm{Re}_\tau^\star/dy)d\overline{u}^{\mathrm{vD}}$, where $d\overline{u}^{\mathrm{vD}} = \sqrt{\overline{\rho}/\rho_w}d(u/u_\tau)$ and $u_\tau = \sqrt{\tau_w/\rho_w}$ is the friction velocity. A mathematically equivalent version of $\overline{u}^\star$ was introduced earlier by Trettel and Larsson [24] using a different route. In the present work, we discuss the influence of variable properties on scaling characteristics of turbulent temperature statistics, and we

TABLE I. Simulation parameters for all cases. $CP395_{Pr1}$, constant property case with $Re_\tau = 395$ and $Pr_w = 1$; $CRe_\tau^\star$, variable property case with constant $Re_\tau^\star$ ($=395$) across the channel; $CRe_\tau^\star CPr^\star$, variable property case with constant $Re_\tau^\star$ ($=395$) and $Pr^\star$ ($=1$) across the channel; GL, case with gaslike density and viscosity variation; $SRe_{\tau GL}^\star$, variable property case with $Re_\tau^\star$ similar to case GL; $GLCPr^\star$, case with gaslike density and viscosity variations and constant $Pr^\star$ ($=1$) across the channel; LL, case with liquidlike viscosity variations; $V\lambda SPr_{LL}^\star$, case with variable thermal conductivity and $Pr^\star$ similar to case LL; and $CP395_{Pr4}$, constant property case with $Re_\tau = 395$ and $Pr_w = 4$.

Case	$\rho(T)$	$\mu(T)$	$\lambda(T)$	$Pr_c^\star$	$Re_{\tau c}^\star$	Line and symbols
$CP395_{Pr1}$	1	1	1	1	395	————
$CRe_\tau^\star$	$(T)^{-1}$	$(T)^{-0.5}$	1	0.71	395	△
$CRe_\tau^\star CPr^\star$	$(T)^{-1}$	$(T)^{-0.5}$	$(T)^{-0.5}$	1	395	□
$SRe_{\tau GL}^\star$	1	$(T)^{1.2}$	1	2.6	152	— —
GL	$(T)^{-1}$	$(T)^{0.7}$	1	1.8	142	○
$GLCPr^\star$	$(T)^{-1}$	$(T)^{0.7}$	$(T)^{0.7}$	1	159	◇
LL	1	$(T)^{-1}$	1	0.56	703	— – —
$V\lambda SPr_{LL}^\star$	1	1	(T)	0.56	395	—— —
$CP395_{Pr4}$	1	1	1	4	395	············

investigate if, similar to velocity statistics, the combined influence of property variations on turbulent temperature statistics can also be parametrized using nondimensional parameters.

II. SIMULATION DETAILS

DNS of fully developed turbulent channel flows are performed using the low-Mach-number approximation of the Navier-Stokes equations without the influence of buoyancy. Using the low-Mach-number approximation, density and other transport properties can be evaluated independently of pressure fluctuations as a function of temperature only [7,25]. The flow is driven by a constant streamwise pressure gradient. Gradients in temperature, and consequently in properties, are achieved using a uniform volumetric heat source. The heat is removed from the two isothermal walls, resulting in averaged temperature and property profiles that are symmetric about the channel center with the maximum average temperature in the middle of the channel. The DNS code discretizes the spatial derivatives in the wall-normal direction using a sixth-order staggered compact finite difference scheme [26,27]. The derivatives in the homogeneous spanwise and streamwise directions are computed using a Fourier expansion with periodic boundary conditions. The time integration is performed using the second-order Adams-Bashforth method. The pressure correction scheme is based on the projection method [28]. Further details on the governing equations can be found in Ref. [15].

A summary of all the simulated cases is given in Table I. The constitutive relations for density ρ, viscosity μ, and thermal conductivity λ as a function of temperature T are given in the second, third, and fourth columns, respectively. The fifth column reports the value of the local mean Prandtl number

$$Pr^\star = Pr_w \frac{(\overline{\mu}/\mu_w)}{(\overline{\lambda}/\lambda_w)} \tag{1}$$

at the channel center and is denoted as $Pr_c^\star$. The semilocal Reynolds number at the channel center, denoted as $Re_{\tau c}^\star$, is given in the sixth column. Note that at the wall $Re_{\tau w}^\star = Re_\tau$ and $Pr_w^\star = Pr_w$. For all simulations, specific heat, c_p, is considered to be constant and the reference friction Reynolds number Re_τ (based on wall quantities) is taken to be 395. The reference Prandtl number Pr_w (also based on wall quantities) for all variable property cases is set to unity. Cases $CP395_{Pr1}$ and $CP395_{Pr4}$ correspond to constant property cases with Prandtl numbers of 1 and 4, respectively. $CRe_\tau^\star$ refers to a variable property case, whose density and viscosity are proportional to $1/T$ and $\sqrt{1/T}$, respectively, such that $Re_\tau^\star$ remains constant across the whole channel. Case $CRe_\tau^\star CPr^\star$ has a similar temperature
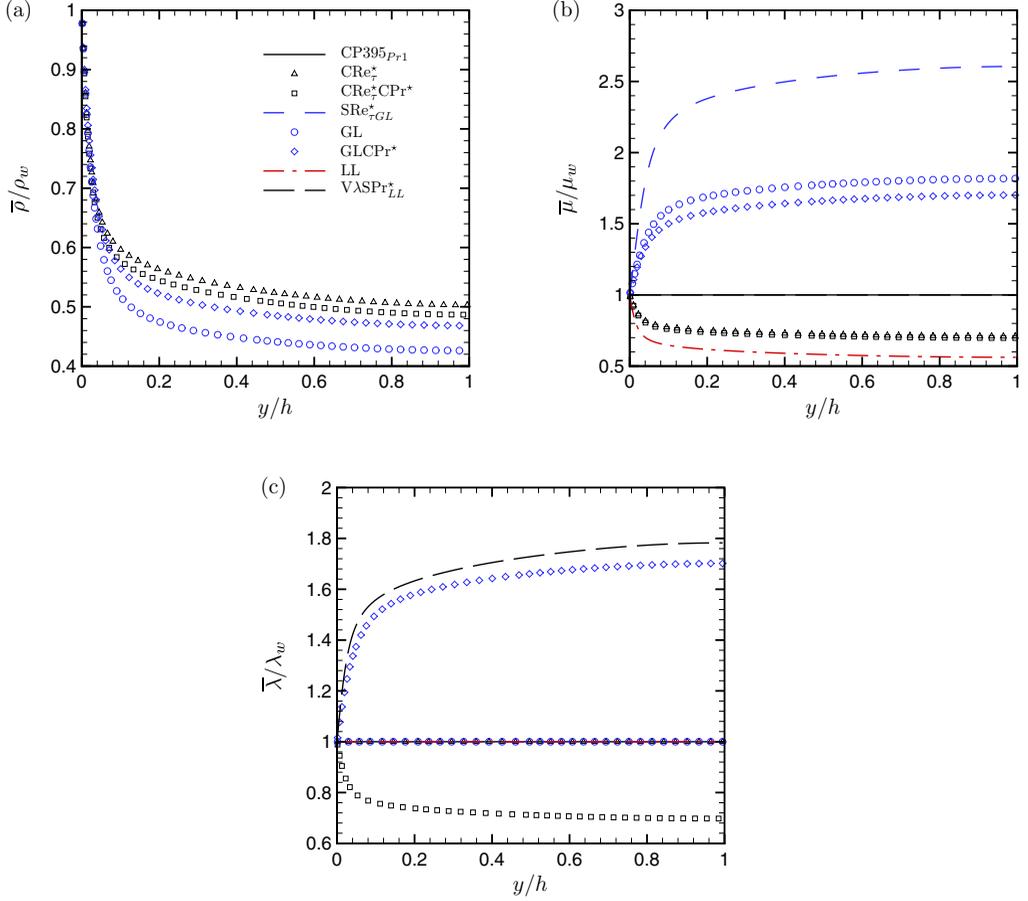
FIG. 1. Averaged (a) density $\overline{\rho}/\rho_w$, (b) viscosity $\overline{\mu}/\mu_w$, and (c) thermal conductivity $\overline{\lambda}/\lambda_w$ as a function of wall-normal distance y/h.

dependency for ρ and μ as case $\text{CRe}_\tau^\star$, while also allowing thermal conductivity to be temperature dependent and equal to viscosity, making the local mean Prandtl number constant across the whole channel. GL corresponds to a gaslike density and viscosity variation. Case $\text{GLCPr}^\star$ has a similar temperature dependency for ρ and μ as case GL and in addition has a constant $\text{Pr}^\star$ across the channel. $\text{SRe}_{\tau\text{GL}}^\star$ refers to a case that has a similar $\text{Re}_\tau^\star$ distribution as case GL. LL corresponds to a case with a liquidlike μ variation. $\text{V}\lambda\text{SPr}_{\text{LL}}^\star$ corresponds to a case with thermal conductivity directly proportional to temperature, such that its $\text{Pr}^\star$ varies but is similar to that of case LL.

Figure 1 shows the distributions of averaged density, viscosity, and thermal conductivity for all cases (except $\text{CP395}_{\text{Pr4}}$). Considerable variations in ρ, μ, and λ are obtained. Cases with variable density are shown as symbols and cases with constant density are shown as lines. Figure 2 shows the distributions of $\text{Re}_\tau^\star$ and $\text{Pr}^\star$. Cases $\text{CP395}_{\text{Pr1}}$, $\text{CP395}_{\text{Pr4}}$, $\text{CRe}_\tau^\star$, $\text{CRe}_\tau^\star\text{CPr}^\star$, and $\text{V}\lambda\text{SPr}_{\text{LL}}^\star$ with constant $\text{Re}_\tau^\star$ across the channel are shown in black. Cases $\text{SRe}_{\tau\text{GL}}^\star$, GL, and $\text{GLCPr}^\star$ with $\text{Re}_\tau^\star$ decreasing away from the wall are shown in blue. Case LL with $\text{Re}_\tau^\star$ increasing away from the wall is shown in red. In the following, the velocity components along the streamwise x, wall-normal y, and spanwise z directions are denoted as u, v, and w, respectively.

Table II lists the maximum grid spacing in terms of the Batchelor scale $\eta_\theta = \eta/\sqrt{\text{Pr}^\star}$ (with η the Kolmogorov scale) for all cases. The values are within the resolution requirements of $\Delta x < 12\eta_\theta$, $\Delta y < 2\eta_\theta$, $\Delta z < 6\eta_\theta$, as also reported in other DNS studies [13,29].
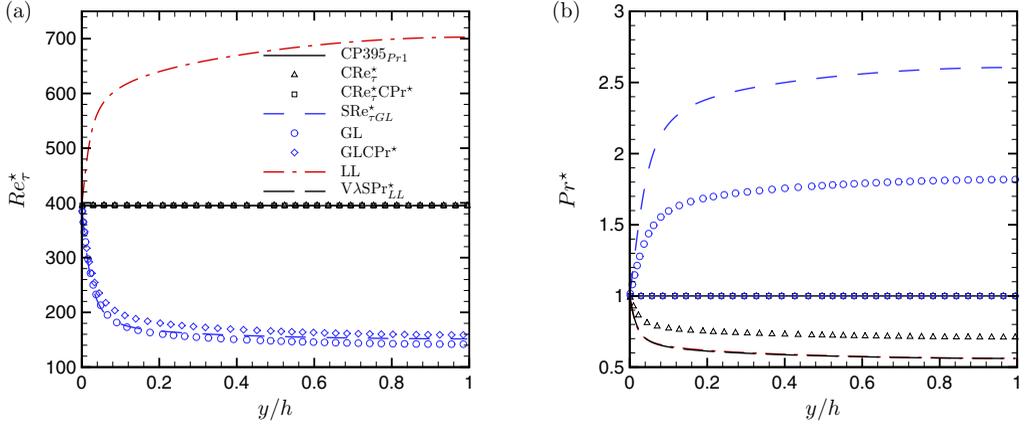
FIG. 2. (a) Semilocal Reynolds number $Re_\tau^\star$ and (b) local Prandtl number $Pr^\star$ as a function of wall-normal distance y/h.

III. SCALAR STATISTICS

As shown in previous works [11,12,15,16,23,24,30], the semilocal wall coordinate $y^\star$ is effective in accommodating changes in viscous scales due to variable properties, thus providing a meaningful representation for the turbulent velocity statistics. Therefore, all wall-normal profiles are plotted as a function of $y^\star$ in the present work.

A. Conventional mean scalar scaling

Figure 3(a) shows the profile of the mean transformed temperature

$$\overline{\theta} = \overline{T} - T_w, \tag{2}$$

normalized by the friction temperature

$$\theta_\tau = \frac{q_w}{\rho_w c_{pw} u_\tau} \tag{3}$$

(q_w is the wall heat flux), for all cases (except case CP395$_{Pr4}$). The constant property case CP395$_{Pr1}$ compares well with the correlation from Kader [18], while all other cases deviate significantly. Using the van Driest transformed temperature profile $\overline{\theta}^{vD} = \int_0^{\overline{\theta}/\theta_\tau} \sqrt{\overline{\rho}/\rho_w} d(\overline{\theta}/\theta_\tau)$, shown in Fig. 3(b), case CRe$_\tau^\star$CPr* (for which both $Re_\tau^\star$ and $Pr^\star$ are a constant) shows a good collapse with case CP395$_{Pr1}$ [see

TABLE II. Maximum spatial resolution, normalized by the Batchelor scale $\eta_\theta = \eta/\sqrt{Pr^\star}$.

Case	$(\Delta x/\eta_\theta)_{\max}$	$(\Delta(y)_{\min}/\eta_\theta)_{\max}$	$(\Delta(y)_{\max}/\eta_\theta)_{\max}$	$(\Delta z/\eta_\theta)_{\max}$
CP395$_{Pr1}$	6.98	0.69	0.89	3.49
CRe$_\tau^\star$	7	0.7	0.74	3.5
CRe$_\tau^\star$CPr*	7	0.7	0.88	3.5
SRe$_{\tau GL}^\star$	10.78	0.64	0.69	4.31
GL	10.8	0.64	0.55	4.31
GLCPr*	10.82	0.65	0.45	4.32
LL	5.6	0.68	0.77	2.8
VλSPr$_{LL}^\star$	6.98	0.69	0.66	3.49
CP395$_{Pr4}$	10.35	0.75	1.34	5.17
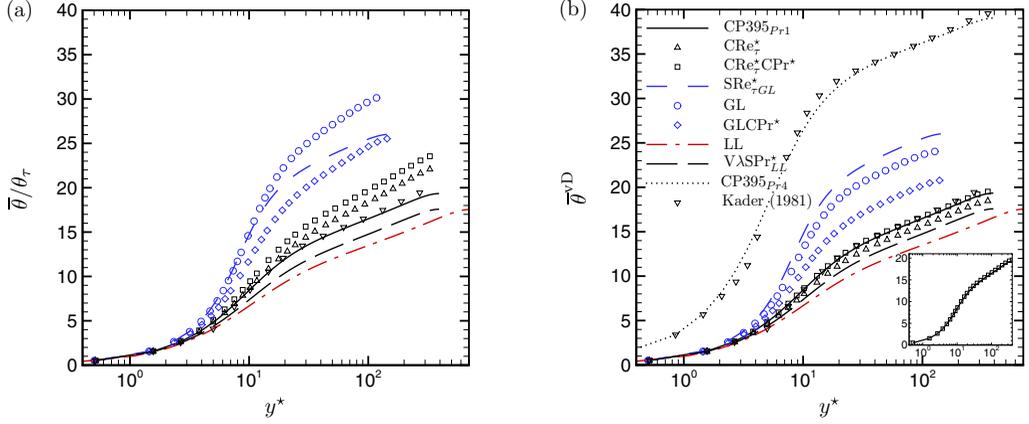
FIG. 3. (a) Mean temperature normalized by friction temperature and (b) van Driest transformed temperature $\overline{\theta}^{\mathrm{vD}}$, plotted as a function of $y^\star$. The inset in panel (b) shows $\overline{\theta}^{\mathrm{vD}}$ for cases $\mathrm{CP395_{Pr1}}$ and $\mathrm{CRe}_\tau^\star\mathrm{CPr}^\star$.

inset of Fig. 3(b)]. Unlike the $\overline{u}^{\mathrm{vD}}$ profiles, which for cases with constant $\mathrm{Re}_\tau^\star$ collapse with constant property cases, a collapse of $\overline{\theta}^{\mathrm{vD}}$ additionally requires $\mathrm{Pr}^\star$ to remain constant. This can be seen for case $\mathrm{CRe}_\tau^\star$ and $\mathrm{V\lambda SPr}_{\mathrm{LL}}^\star$, for which $\mathrm{Re}_\tau^\star$ is a constant but $\mathrm{Pr}^\star$ varies, therefore showing deviation from case $\mathrm{CP395_{Pr1}}$. A Prandtl-number-dependent shift also occurs when comparing profiles of $\overline{\theta}/\theta_\tau$ for constant property cases at different Prandtl numbers, as can be seen by comparing case $\mathrm{CP395_{Pr1}}$ with $\mathrm{CP395_{Pr4}}$ (also see, e.g., Ref. [2]). Similar to $\overline{u}^{\mathrm{vD}}$, which does not collapse for cases with $\mathrm{Re}_\tau^\star$ gradients, $\overline{\theta}^{\mathrm{vD}}$ also deviates significantly for cases with $\mathrm{Re}_\tau^\star$ gradients. This can be seen for the case $\mathrm{GLCPr}^\star$, for which $\mathrm{Pr}^\star$ is constant and $\mathrm{Re}_\tau^\star$ varies. Cases $\mathrm{SRe}_{\tau\mathrm{GL}}^\star$, GL, and LL experience the combined effect of variations in both $\mathrm{Pr}^\star$ and $\mathrm{Re}_\tau^\star$.

Lee *et al.* [17], who investigated heated turbulent boundary layers with variable viscosity, proposed a modification to Kader's original relation [18] for the mean scalar distribution by accounting for variations in local Prandtl number. The relation is given as

$$\overline{\theta}^{\mathrm{vD}} = \mathrm{Pr}^\star y^\star \exp(-\Gamma) + \left\{2.12\ln\left[(1+y^\star)\frac{1.5(2-y/h)}{1+2(1-y/h)^2}\right] + \beta(\mathrm{Pr}_v)\right\}\exp(-1/\Gamma), \quad (4)$$

with

$$\beta(\mathrm{Pr}_v) = \left(3.85\mathrm{Pr}_v^{1/3} - 1.3\right)^2 + 2.12\ln\mathrm{Pr}_v \qquad (5)$$

and

$$\Gamma = \frac{10^{-2}(\mathrm{Pr}^\star y^\star)^4}{1 + 5\mathrm{Pr}^{\star 3}y^\star} \quad \text{and} \quad \mathrm{Pr}_v = \mathrm{Pr}^\star(y^\star \approx 30). \qquad (6)$$

They proposed that except for the definition of β, all Pr values in the original relation by Kader should be replaced by $\mathrm{Pr}^\star$ and the inner-scaled wall coordinate should be $y^\star$ instead of y^+. For defining β, which determines the elevation of the log-law, they proposed to use the Prandtl number at the start of the log region $\mathrm{Pr}_v = \mathrm{Pr}^\star(y^\star \approx 30)$.

A comparison of the proposed relation for selected cases is shown in Fig. 4(a). A close approximation is provided for cases with decreasing $\mathrm{Re}_\tau^\star$ and increasing $\mathrm{Pr}^\star$ ($\mathrm{SRe}_{\tau\mathrm{GL}}^\star$, GL) or vice versa (LL). The prediction for cases where only one of the parameters ($\mathrm{Re}_\tau^\star$ or $\mathrm{Pr}^\star$) varies ($\mathrm{CRe}_\tau^\star$, $\mathrm{GLCPr}^\star$, $\mathrm{V\lambda SPr}_{\mathrm{LL}}^\star$) is in general poor. This can be clearly seen for case $\mathrm{GLCPr}^\star$ [see inset of Fig. 4(a)], where because of constant $\mathrm{Pr}^\star$, Eq. (4) provides a similar distribution as case $\mathrm{CP395_{Pr1}}$. However, $\overline{\theta}^{\mathrm{vD}}$ for $\mathrm{GLCPr}^\star$ is much higher. This nonuniversal behavior can be attributed to the fact that Eq. (4) assumes that the slope of the log-law is unaffected by property variations, which is not
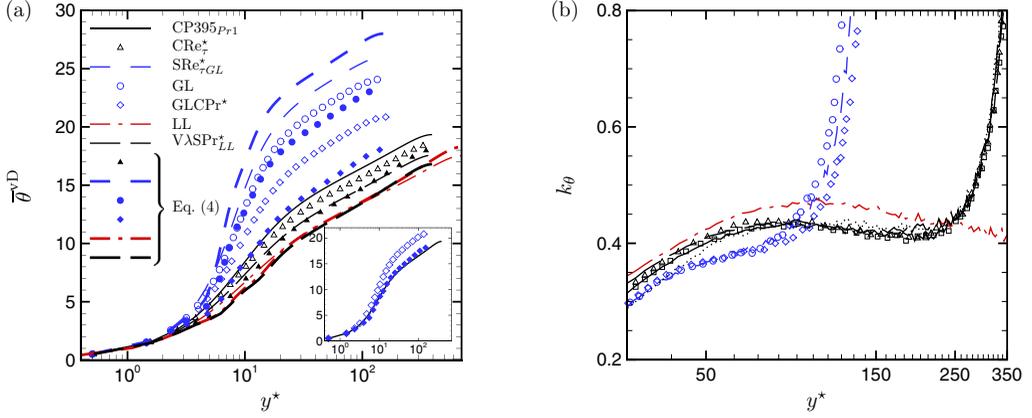
FIG. 4. (a) van Driest transformed temperature $\overline{\theta}^{\mathrm{vD}}$ from DNS (open symbols and thin lines) compared with the modified Kader correlation as suggested by Lee *et al.* [17] (closed symbols and thick lines) and (b) von Karman constant k_θ for the van Driest transformed temperature profile, plotted as a function of $y^\star$. The inset in panel (a) shows $\overline{\theta}^{\mathrm{vD}}$ from DNS for cases CP395$_{\mathrm{Pr1}}$ and GLCPr* compared with prediction from Eq. (4).

the case for cases with Re$_\tau^\star$ gradients as can be seen by the diagnostic function that is related with the inverse of the slope of the log-law k_θ as

$$\frac{1}{k_\theta} = y^\star \frac{d\overline{\theta}^{\mathrm{vD}}}{dy^\star}. \tag{7}$$

A plot of k_θ is shown in Fig. 4(b). It is noticeable that k_θ increases with increasing Re$_\tau^\star$ and decreases with decreasing Re$_\tau^\star$ away from the wall. Clearly, the distribution of $\overline{\theta}^{\mathrm{vD}}$ is influenced by Re$_\tau^\star$ gradients.

B. Re$_\tau^\star$ invariant mean scalar scaling

In order to account for Re$_\tau^\star$ variations and to further investigate the characteristics of mean temperature profiles, we first introduce the mean heat flux equation. The relation for the wall-normal turbulent heat flux and conductive heat flux can be obtained by integrating the mean energy equation, which for a fully developed turbulent channel flow, can be written as

$$-\frac{\overline{\rho}\widetilde{v''\theta''}}{\rho_w u_\tau \theta_\tau} + \frac{h}{\mathrm{Re}_\tau \mathrm{Pr}_w} \left(\frac{\overline{\lambda}}{\lambda_w}\right) \frac{d(\overline{\theta}/\theta_\tau)}{dy} + \frac{h}{\mathrm{Re}_\tau} \overline{\left(\frac{\lambda'}{\lambda_w}\right) \frac{d(\theta'/\theta_\tau)}{dy}} = \left(1 - \frac{y}{h}\right). \tag{8}$$

In the above equation, the prime and double prime denote fluctuations using Reynolds and Favre decomposition, respectively, while the tilde denotes Favre averaging. Neglecting the thermal conductivity fluctuations in Eq. (8) gives

$$-\frac{\overline{\rho}\widetilde{v''\theta''}}{\rho_w u_\tau \theta_\tau} + \frac{h}{\mathrm{Re}_\tau \mathrm{Pr}_w} \left(\frac{\overline{\lambda}}{\lambda_w}\right) \frac{d(\overline{\theta}/\theta_\tau)}{dy} \approx \left(1 - \frac{y}{h}\right). \tag{9}$$

Using the turbulent eddy conductivity

$$\alpha_t = -\frac{\overline{\rho}\widetilde{v''\theta''}}{\left(\frac{d\overline{\theta}}{dy}\right)}, \tag{10}$$
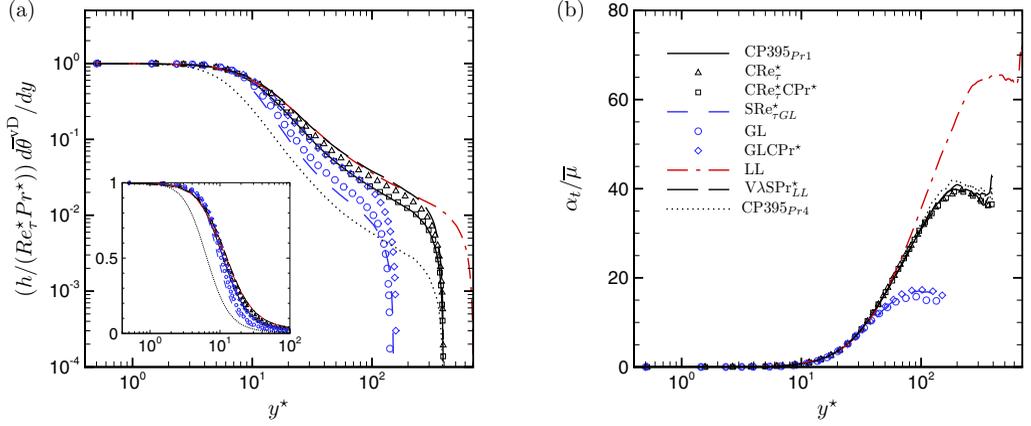
FIG. 5. (a) Conductive heat flux and (b) turbulent eddy conductivity normalized by mean viscosity, plotted as a function of $y^\star$.

Eq. (9) can be written as

$$\left[\frac{\alpha_t}{\mu_w} + \frac{1}{\mathrm{Pr}_w}\left(\frac{\overline{\lambda}}{\lambda_w}\right)\right]\frac{h}{\mathrm{Re}_\tau}\frac{d(\overline{\theta}/\theta_\tau)}{dy} \approx \left(1 - \frac{y}{h}\right). \qquad (11)$$

The above equation can then further be expressed in terms of semilocal parameters, $\mathrm{Re}_\tau^\star$ and $\mathrm{Pr}^\star$, and the van Driest mean temperature increment

$$d\overline{\theta}^{\mathrm{vD}} = \sqrt{\frac{\overline{\rho}}{\rho_w}}d\left(\frac{\overline{\theta}}{\theta_\tau}\right) \qquad (12)$$

to give

$$\left(\frac{\alpha_t}{\overline{\mu}} + \frac{1}{\mathrm{Pr}^\star}\right)\frac{h}{\mathrm{Re}_\tau^\star}\frac{d\overline{\theta}^{\mathrm{vD}}}{dy} \approx \left(1 - \frac{y}{h}\right). \qquad (13)$$

A plot of the conductive heat flux $[h/(\mathrm{Re}_\tau^\star\mathrm{Pr}^\star)]d\overline{\theta}^{\mathrm{vD}}/dy$, as a function of $y^\star$ is shown in Fig. 5(a). The plot provides a measure of the conductive sublayer thickness. For constant property cases, it can be clearly seen that the conduction dominated region reduces for case CP395$_{\mathrm{Pr4}}$, when compared with case CP395$_{\mathrm{Pr1}}$. For variable property cases, an increase in $\mathrm{Pr}^\star$ toward the channel center (cases SRe$_{\tau\mathrm{GL}}^\star$ and GL) reduces the thickness of the conduction dominated region in terms of $y^\star$, while the reverse happens when $\mathrm{Pr}^\star$ decreases (cases CRe$_\tau^\star$, LL and VλSPr$_{\mathrm{LL}}^\star$). The case GLCPr* with constant $\mathrm{Pr}^\star = 1$ and variable $\mathrm{Re}_\tau^\star$, shows a good collapse with case CP395$_{\mathrm{Pr1}}$ over the entire inner layer. This behavior is similar to constant property cases with the same Pr_w, but different Re_τ values (see, e.g., Ref. [2]). Similarly, cases LL and VλSPr$_{\mathrm{LL}}^\star$, which exhibit quasisimilar $\mathrm{Pr}^\star$ profiles, also show quasisimilar conductive heat flux profiles, despite the different $\mathrm{Re}_\tau^\star$ profiles. All the above observations can be summarized mathematically by investigating the scaling characteristics of the turbulent eddy conductivity. A plot of $\alpha_t/\overline{\mu}$ as a function of $y^\star$ in Fig. 5(b) shows a reasonable collapse in the inner layer for all cases. While we will discuss this collapse later in more detail, the direct implication of this collapse will be discussed first. Since in the overlap region, located between the buffer layer and the channel core, the turbulent mixing dominates (i.e., $\alpha_t/\overline{\mu} \gg 1/\mathrm{Pr}^\star$, and the inner scaling applies), Eq. (13) gives

$$\frac{h}{\mathrm{Re}_\tau^\star}\frac{d\overline{\theta}^{\mathrm{vD}}}{dy} = \Phi(y^\star), \qquad (14)$$
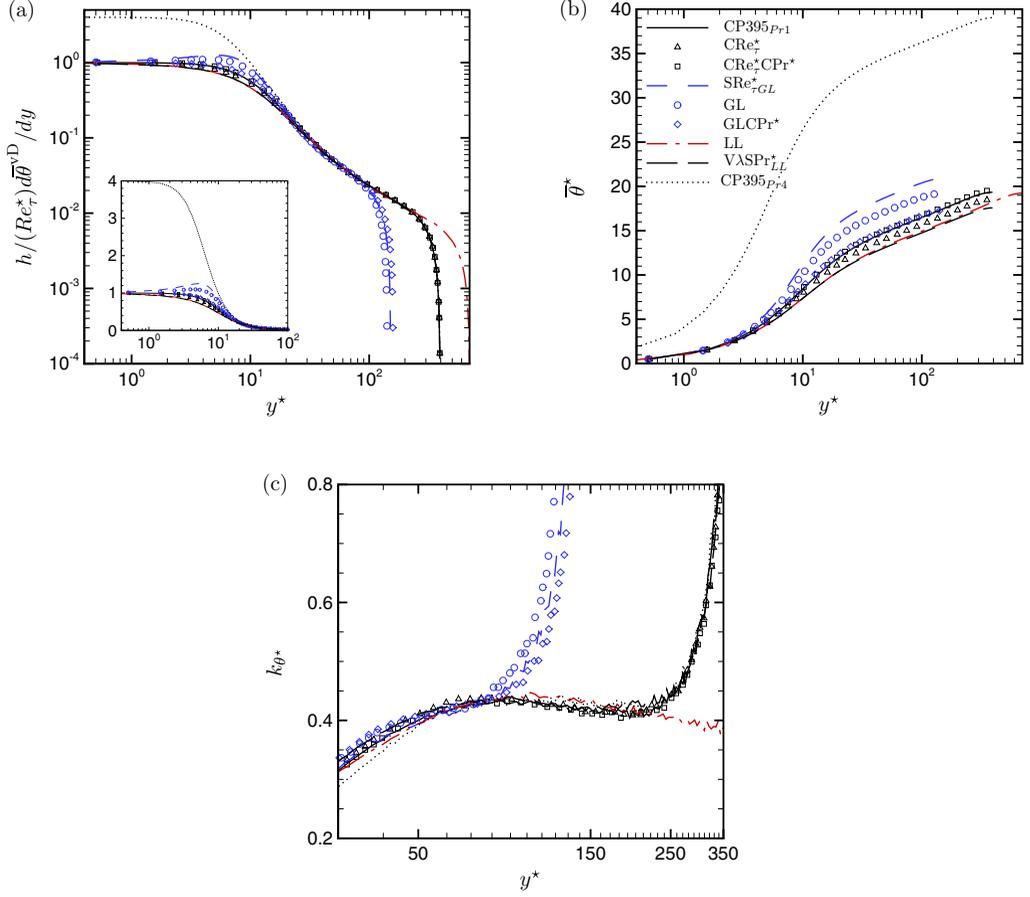
FIG. 6. (a) van Driest temperature gradient normalized by the semilocal viscous length scale, (b) extended van Driest transformed temperature, and (c) von Karman constant $k_{\theta^\star}$ for the extended van Driest transformed temperature profile, plotted as a function of $y^\star$.

where Φ is an unknown function of $y^\star$. A plot of the van Driest temperature gradient normalized by the semilocal length scale is shown in Fig. 6(a) as a function of $y^\star$. A good collapse is obtained in the entire inner layer, except in regions where molecular effects are dominant ($y^\star < 30$ for the present cases). The effectiveness of this collapse can be used to extend the van Driest transformed temperature to provide a temperature profile that exhibits similar characteristics as the ones of a constant property case. Following a similar procedure we used to derive $\overline{u}^\star$ in Ref. [16], Eq. (14) can be written as

$$\frac{h}{\mathrm{Re}_\tau^\star}\left(\frac{dy^\star}{dy}\right)\frac{d\overline{\theta}^{\mathrm{vD}}}{dy^\star} = \Phi(y^\star). \tag{15}$$

$dy^\star/dy$ can be obtained by taking the derivative of $y^\star = y\mathrm{Re}_\tau^\star/h$ with respect to y, to obtain

$$\left(1 + \frac{y}{\mathrm{Re}_\tau^\star}\frac{d\mathrm{Re}_\tau^\star}{dy}\right)\frac{d\overline{\theta}^{\mathrm{vD}}}{dy^\star} = \Phi(y^\star). \tag{16}$$

Equation (16) can then be written in terms of the extended van Direst temperature profile increment $d\overline{\theta}^{\star}$ as

$$\frac{d\overline{\theta}^{\star}}{dy^{\star}} = \left(1 + \frac{y}{\mathrm{Re}_{\tau}^{\star}}\frac{d\mathrm{Re}_{\tau}^{\star}}{dy}\right)\frac{d\overline{\theta}^{\mathrm{vD}}}{dy^{\star}} = \Phi(y^{\star}). \tag{17}$$

The last equality in this equation is valid only in the overlap region. In the region close to the wall (assuming a constant heat flux region), $d\overline{\theta}^{\star}/dy^{\star}$ is given as

$$\frac{d\overline{\theta}^{\star}}{dy^{\star}} = \frac{h}{\mathrm{Re}_{\tau}^{\star}}\frac{d\overline{\theta}^{\mathrm{vD}}}{dy} = \frac{1}{\left(\frac{\alpha_t}{\overline{\mu}} + \frac{1}{\mathrm{Pr}^{\star}}\right)}. \tag{18}$$

Therefore, $\overline{\theta}^{\star} = \int_0^{\overline{\theta}^{\mathrm{vD}}}(1 + (y/\mathrm{Re}_{\tau}^{\star})d\mathrm{Re}_{\tau}^{\star}/dy)d\overline{\theta}^{\mathrm{vD}}$ (obtained by integrating from the wall), exhibits a $\mathrm{Pr}^{\star}$-dependent shift. A plot of $\overline{\theta}^{\star}$, as a function of $y^{\star}$, is shown in Fig. 6(b). It can be seen that all cases with $\mathrm{Pr}^{\star} = 1$ (CP395$_{\mathrm{Pr1}}$, CRe$_{\tau}^{\star}$CPr*, and GLCPr*) show a reasonable collapse, irrespective of the Re$_{\tau}^{\star}$ profile. Similarly, case LL and VλSPr$_{\mathrm{LL}}^{\star}$, with quasisimilar $\mathrm{Pr}^{\star}$ variations, exhibit similar $\overline{\theta}^{\star}$ profiles. Additionally, all cases exhibit a similar slope in the log-law region, which can be seen by the plot of the inverse of the log-law slope $k_{\theta^{\star}}$, given by

$$\frac{1}{k_{\theta^{\star}}} = y^{\star}\frac{d\overline{\theta}^{\star}}{dy^{\star}}, \tag{19}$$

which is shown in Fig. 6(c). $\overline{\theta}^{\star}$ therefore exhibits all characteristics of a constant property scalar distribution (for $\mathrm{Pr}_w > 0.2$), which also have a Prandtl-number-dependent shift and a similar slope in the log-law region, irrespective of their Re$_{\tau}$ and Pr_w values. The origin of the log-law region in terms of $y^{\star}$ is also found to remain invariant for the cases presented herein.

The universal nature of $\overline{\theta}^{\star}$ and its Prandtl-number-dependent shift can further be quantified by splitting $d\overline{\theta}^{\star}/dy^{\star}$ into a $\alpha_t/\overline{\mu}$-dependent term and a term that exists because of a nonunity Prandtl number, as

$$\frac{d\overline{\theta}^{\star}}{dy^{\star}} \approx \frac{1 - y/h}{\left(\frac{\alpha_t}{\overline{\mu}} + \frac{1}{\mathrm{Pr}^{\star}}\right)} = \frac{1 - y/h}{\left(\frac{\alpha_t}{\overline{\mu}} + 1\right)} + \sum_{n=1}^{\infty}\frac{(1 - y/h)(-1 + \mathrm{Pr}^{\star})^n\left(\frac{-\alpha_t/\overline{\mu}}{\alpha_t/\overline{\mu}+1}\right)^{-1+n}}{\left(\frac{\alpha_t}{\overline{\mu}} + 1\right)^2}, \tag{20}$$

which after integration gives

$$\overline{\theta}^{\star} \approx \int_0^{y^{\star}}\frac{1 - y/h}{\left(\frac{\alpha_t}{\overline{\mu}} + \frac{1}{\mathrm{Pr}^{\star}}\right)}dy^{\star}$$

$$= \underbrace{\int_0^{y^{\star}}\frac{1 - y/h}{\left(\frac{\alpha_t}{\overline{\mu}} + 1\right)}dy^{\star}}_{\overline{\theta}_{\mathcal{T}}^{\star}} + \underbrace{\int_0^{y^{\star}}\sum_{n=1}^{\infty}\frac{(1 - y/h)(-1 + \mathrm{Pr}^{\star})^n\left(\frac{-\alpha_t/\overline{\mu}}{\alpha_t/\overline{\mu}+1}\right)^{-1+n}}{\left(\frac{\alpha_t}{\overline{\mu}} + 1\right)^2}dy^{\star}}_{\overline{\theta}_{\mathcal{P}}^{\star}}. \tag{21}$$

A good universal collapse of $\overline{\theta}_{\mathcal{T}}^{\star}$ in the inner layer can be seen in Fig. 7(a). The Prandtl-number-dependent shift occurring because of nonunity $\mathrm{Pr}^{\star}$ can be seen using $\overline{\theta}_{\mathcal{P}}^{\star}$ in Fig. 7(b). The profile becomes flattened in the overlap layer, indicating the dominance of $\alpha_t/\overline{\mu} \gg 1/\mathrm{Pr}^{\star}$.

C. Turbulent Prandtl number

The success of the extended van Driest transformed temperature $\overline{\theta}^{\star}$ is further investigated by studying the analogy between momentum transfer and scalar transport. Patel *et al.* [16] showed that the viscous stress $h/\mathrm{Re}_{\tau}^{\star}(d\overline{u}^{\mathrm{vD}}/dy)$ collapses reasonably well when plotted as a function of $y^{\star}$.
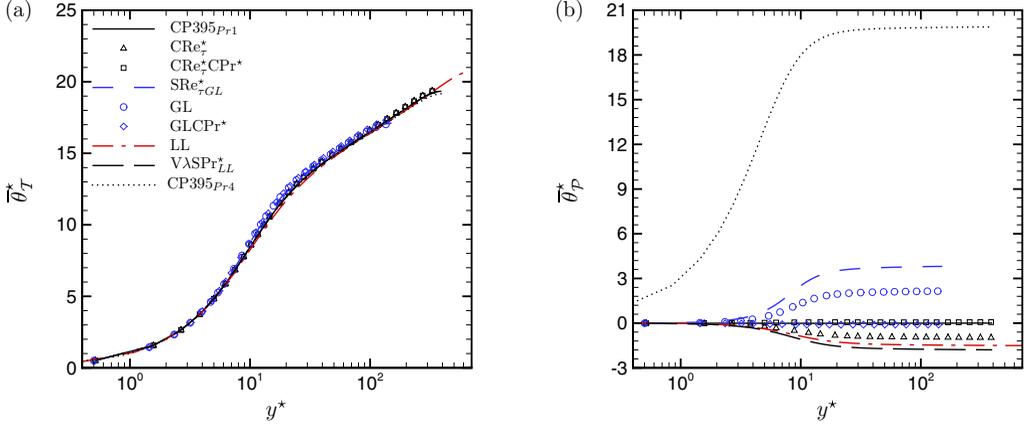
FIG. 7. Decomposition of $\overline{\theta}^\star$ into (a) $\overline{\theta}^\star_{\mathcal{T}}$ and (b) $\overline{\theta}^\star_{\mathcal{P}}$, as given in Eq. (21).

For the near-wall constant stress layer, this collapse can be written in terms of the turbulent eddy viscosity μ_t as

$$\frac{h}{\mathrm{Re}^\star_\tau} \frac{d\overline{u}^{\mathrm{vD}}}{dy} = \frac{1}{\left(\frac{\mu_t}{\overline{\mu}} + 1\right)} = \Psi(y^\star), \tag{22}$$

where Ψ is an unknown function of $y^\star$. This results in $\mu_t/\overline{\mu}$ to be a universal function of $y^\star$ in the inner layer. A plot of $\mu_t/\overline{\mu}$ is shown along with $\alpha_t/\overline{\mu}$ as a function of $y^\star$ in Fig. 8(a). It can be seen that the profiles of $\mu_t/\overline{\mu}$ and $\alpha_t/\overline{\mu}$ behave similarly, showing a strong analogy between turbulent momentum transfer and scalar transport. This is also seen in Fig. 8(b), where the turbulent Prandtl number Pr_t is shown. Pr_t varies slightly around unity in the inner layer, indicating again the strong analogy between momentum transfer and scalar transport. This, along with the universal behavior of $\overline{u}^\star$ are the reasons for the success of $\overline{\theta}^\star$.

A closer inspection of the near-wall behavior of $\mu_t/\overline{\mu}$ and $\alpha_t/\overline{\mu}$ shows deviations in the region $y^\star < 10$ for cases with $\mathrm{Re}^\star_\tau$ gradients. This deviation in $\mu_t/\overline{\mu}$ was noted by Patel *et al.* [16] as a deviation in mixing length and stems from turbulence modulation occurring in cases with $\mathrm{Re}^\star_\tau$ gradients, which influence the anisotropy of the turbulence and also alter the Reynolds stress generation mechanism. This change in anisotropy also influences the turbulent heat flux generation mechanism and is discussed in the next section. The influence of this near-wall deviation in $\mu_t/\overline{\mu}$ on scaling of $\overline{u}^\star$ was found to be negligible for the present cases, since the deviations were limited to the viscous dominated region. A similar analysis is done for $\overline{\theta}^\star$ in Fig. 8(c) by comparing $\alpha_t/\overline{\mu}$ with $1/\mathrm{Pr}^\star$. It can be seen that for the present cases the influence of turbulence modulation does not influence $\overline{\theta}^\star$ and its shift in the overlap layer is only because of $\mathrm{Pr}^\star$. However, this change in near-wall behavior of $\alpha_t/\overline{\mu}$ for cases with $\mathrm{Re}^\star_\tau$ gradients could play a crucial role in scalar transport for high-Prandtl-number fluids, for which the cross-over point between $1/\mathrm{Pr}^\star$ and $\alpha_t/\overline{\mu}$ moves closer to the wall.

D. Joint probability density function

This section discusses how the streamwise and wall-normal turbulent heat flux are affected by turbulence modulation due to gradients in $\mathrm{Re}^\star_\tau$, and by variations in $\mathrm{Pr}^\star$. For this analysis, we will use contours of weighted joint probability density functions (JPDF's), $\rho u'' \theta'' P[\sqrt{\rho}\theta''/(\sqrt{\rho_w}\theta_\tau), \sqrt{\rho}u''/(\sqrt{\rho_w}u_\tau)]/(\rho_w \theta_\tau u_\tau)$ and $\rho v'' \theta'' P[\sqrt{\rho}\theta''/(\sqrt{\rho_w}\theta_\tau, \sqrt{\rho}v''/(\sqrt{\rho_w}u_\tau))]/(\rho_w \theta_\tau u_\tau)$, where $P(\mathcal{X},\mathcal{Y})$ represents the JPDF of $\mathcal{X}$ and $\mathcal{Y}$. Note that their surface integrals give the streamwise and wall-normal turbulent heat fluxes, respectively.
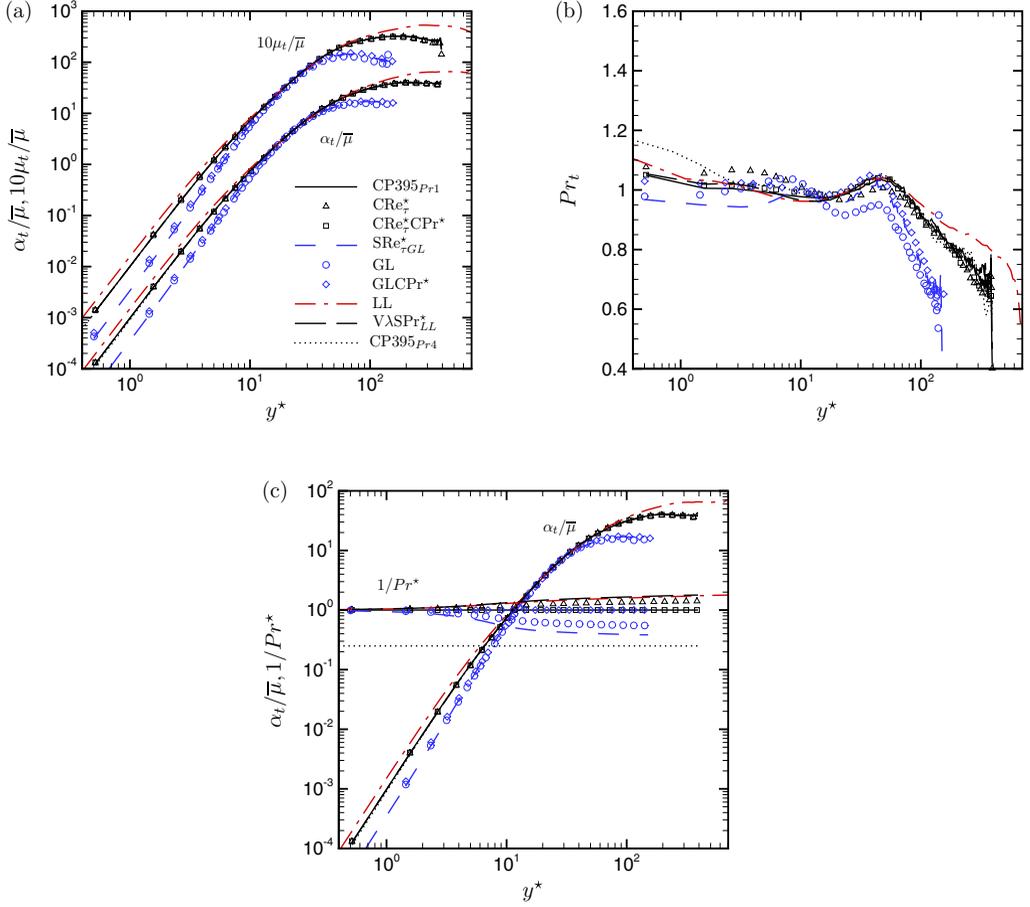
FIG. 8. (a) Turbulent eddy conductivity and turbulent eddy viscosity (multiplied by 10 for visualization purposes) normalized by mean viscosity, (b) turbulent Prandtl number, and (c) turbulent eddy conductivity normalized by mean viscosity and inverse of local mean Prandtl number, plotted as a function of $y^\star$.

Figure 9 shows contours of the weighted JPDF for the streamwise turbulent heat flux in the left column [Figs. 9(a), 9(c) 9(e), and 9(g)] and the wall-normal turbulent heat flux in the middle column [Figs. 9(b), 9(d) 9(f), and 9(h)]. Both JPDF's are taken at $y^\star \approx 12$. The last column shows the $Re_\tau^\star$ and $Pr^\star$ distributions of the variable property cases that are compared with the reference constant property case CP395$_{Pr1}$. For all the plots, the filled contours depict the constant property case and the variable property cases are shown as lines. The variable property cases in the rows from top to bottom are CRe$_\tau^\star$CPr* (variable property case with constant $Re_\tau^\star$ and $Pr^\star$), GLCPr* (constant $Pr^\star$, but $Re_\tau^\star$ decreases away from the wall), VλSPr$_{LL}^\star$ (constant $Re_\tau^\star$, but $Pr^\star$ decreasing away from the wall), and case GL (increasing $Pr^\star$, and decreasing $Re_\tau^\star$ away from the wall).

The turbulence modulation due to $Re_\tau^\star$ gradients can be seen in the first and second row. If $Re_\tau^\star$ is constant, the streamwise and wall-normal turbulent heat fluxes [Figs. 9(a) and 9(b)] are similar to the constant property case CP395$_{Pr1}$, irrespective of the individual property gradients. However, if $Re_\tau^\star$ decreases, the low-speed streaks strengthen and the corresponding correlated low-temperature fluctuations increase in intensity, as evidently seen in the weighted JPDF for the streamwise turbulent heat flux [Figs. 9(c)]. This behavior is in contrast to the Reynolds number effect and is associated with changes in turbulence structure due to $Re_\tau^\star$ gradients. The change in turbulence structure is further
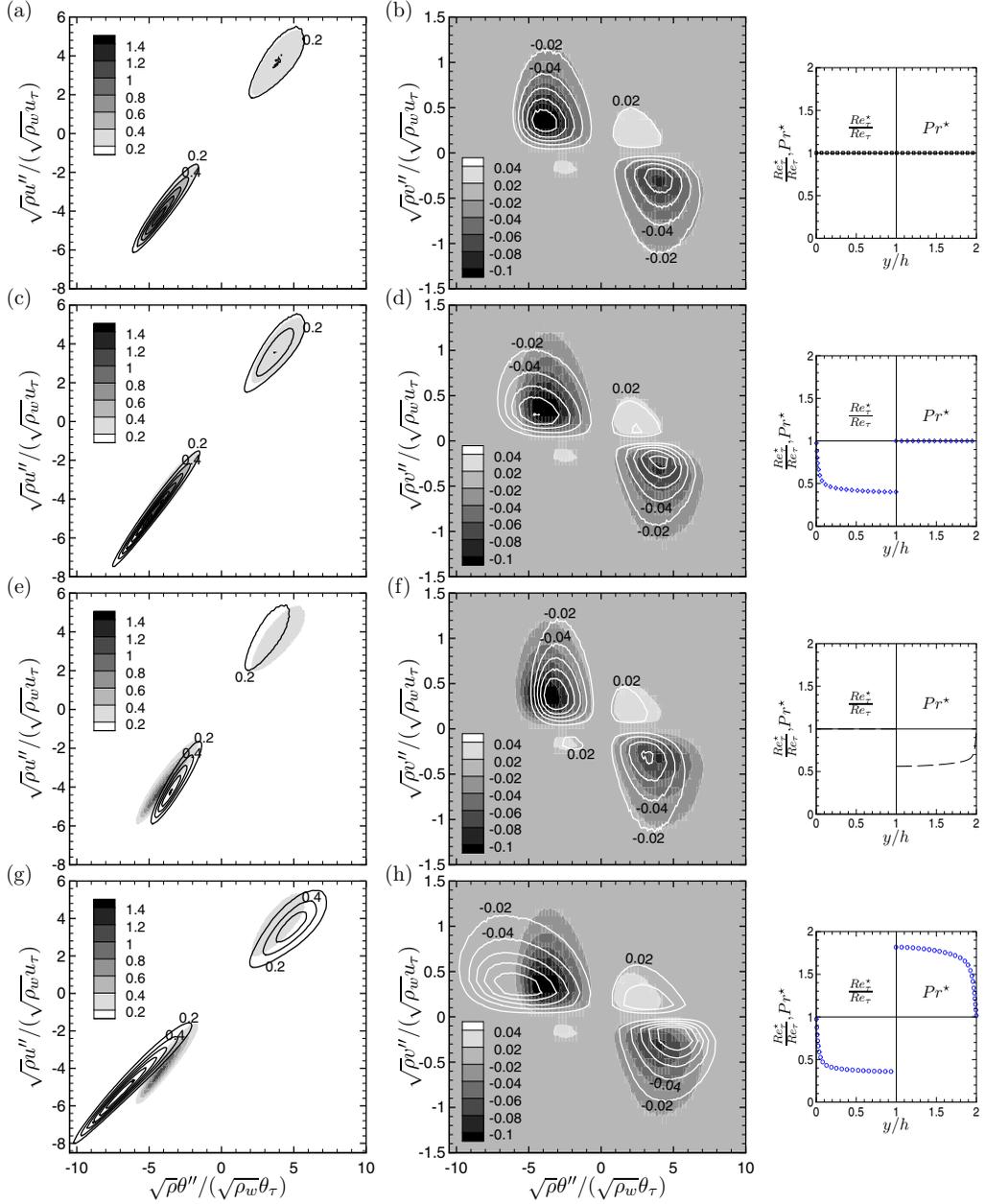
FIG. 9. Weighted joint probability density functions at $y^\star \approx 12$ of [(a), (c), (e), (g)] streamwise turbulent heat flux, $\rho u'' \theta'' P(\sqrt{\rho}\theta'', \sqrt{\rho}u'')$, and [(b), (d), (f), (h)] wall-normal turbulent heat flux, $\rho v'' \theta'' P(\sqrt{\rho}\theta'', \sqrt{\rho}v'')$. The last column gives an overview of the $Re_\tau^\star$ and $Pr^\star$ profiles for the variable property cases. The filled contours correspond to the reference constant property case $CP395_{Pr1}$ and the lines correspond to case $CRe_\tau^\star CPr^\star$ [(a), (b)], $GLCPr^\star$ [(c), (d)], $V\lambda SPr^\star_{LL}$ [(e), (f)], and GL [(g), (h)].

indicated by the weighted JPDF for the wall-normal turbulent heat flux, where the low-temperature fluctuations do not lift as intensely as in case $CP395_{Pr1}$ [Fig. 9(d)].

The influence of $Pr^\star$ variations on the JPDFs can been seen in the third row. Case $V\lambda SPr^\star_{LL}$, for which $Pr^\star$ decreases away from the wall, results in weaker scalar fluctuations and thus results in an
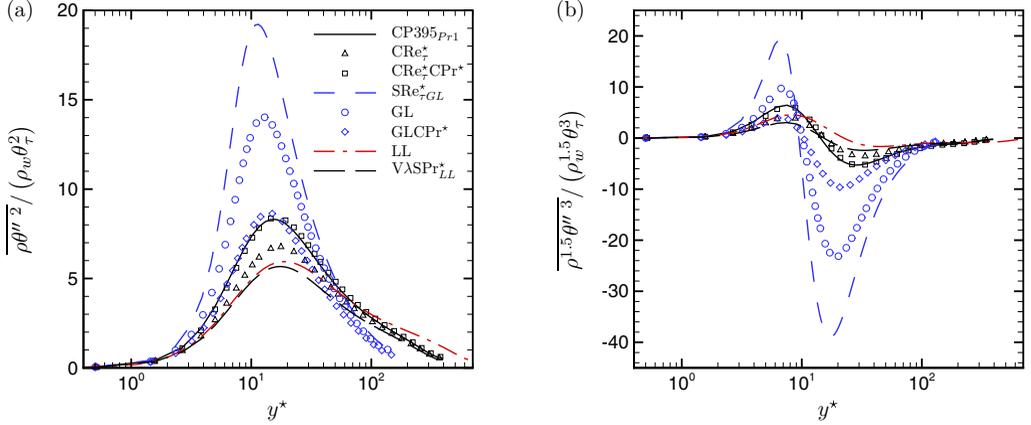
FIG. 10. (a) Second-order and (b) third-order temperature fluctuations, plotted as a function of $y^\star$.

higher slope of the JPDF for the streamwise turbulent heat flux [Fig. 9(e)] and a horizontal shift of the JPDF for the wall-normal turbulent heat flux [Fig. 9(f)] toward weaker scalar fluctuations. The combined effect of both $Re_\tau^\star$ and $Pr^\star$ variations can be seen in the fourth row. The increase in $Pr^\star$ for case GL results in a lower slope of the weighted JPDF for the streamwise turbulent heat flux [Fig. 9(g)], while the decrease in $Re_\tau^\star$ results in stretching the JPDF in the third quadrant since the low-speed streaks and the corresponding correlated low-temperature fluctuations strengthen. The weighted JPDF for the wall-normal turbulent heat flux [Fig. 9(h)] shifts horizontally toward higher scalar fluctuations due to the increase in $Pr^\star$, while the decrease in $Re_\tau^\star$ causes the low-temperature fluctuations to lift less intensely than in case CP395$_{Pr1}$.

E. Higher order scalar statistics

Higher order statistics of the scalar field will be discussed next. Using the semilocal framework, the appropriate forms of second- and third-order temperature fluctuations involve a density-weighted correction and are given by $\overline{\rho\theta''^2}/(\rho_w\theta_\tau^2)$ [Fig. 10(a)] and $\overline{\rho^{1.5}\theta''^3}/(\rho_w^{1.5}\theta_\tau^3)$ [Fig. 10(b)], respectively. From constant property studies [4], it is known that the scalar fluctuation statistics show a strong Prandtl-number dependency, while the Reynolds-number dependency, although present, is weak. A similar behavior can be seen for the present cases, where for cases with increasing $Pr^\star$ (SRe$_{\tau GL}^\star$ and GL) the peaks become more pronounced, while the reverse happens for cases with decreasing $Pr^\star$ (CRe$_\tau^\star$, LL, VλSPr$_{LL}^\star$). The statistics for cases with constant $Pr^\star$ show a good collapse only when the $Re_\tau^\star$ profiles are also similar (see, e.g., cases CP395$_{Pr1}$ and CRe$_\tau^\star$CPr*), while small deviations are observed when $Re_\tau^\star$ differs (see, e.g., CP395$_{Pr1}$ and GLCPr*). This $Re_\tau^\star$-dependent deviation is even more pronounced for third-order statistics. Similar observations can be made for cases LL and VλSPr$_{LL}^\star$, which have quasisimilar $Pr^\star$ but different $Re_\tau^\star$. Although not shown here, it should be noted that, similar to statistics of velocity fluctuations discussed by Patel *et al.* [15], it was found that $\overline{\rho\theta''^2} \approx \overline{\rho\theta''^2}$, but $\overline{\rho^{1.5}\theta''^3} \neq \overline{\rho^{1.5}\theta''^3}$. This highlights the importance of including density fluctuations in third-order moments, because of the functional relation between density and temperature, which causes a preferential concentration of a high-density fluid in a low-temperature streak, and vice versa.

IV. CONCLUSION

DNS of fully developed channel flows under the low-Mach-number approximation of the Navier-Stokes equations are performed using different constitutive relations for density, viscosity, and thermal conductivity to study the scaling characteristics of a turbulent scalar field. In addition to the distribution of the semilocal Reynolds number $Re_\tau^\star$, also the distribution of the local Prandtl

number $\Pr^\star \equiv \Pr_w (\overline{\mu}/\mu_w)/(\overline{\lambda}/\lambda_w)$ plays an important role in scaling of scalar statistics. The van Driest transformed mean temperature profiles $\overline{\theta}^{\mathrm{vD}}$ for variable property cases collapse with the constant property mean scalar distribution (with Prandtl number $\Pr_w$) only when their $\mathrm{Re}_\tau^\star$ and $\Pr^\star$ distributions are constant across the channel. Near-wall gradients in $\mathrm{Re}_\tau^\star$ result in deviations of $\overline{\theta}^{\mathrm{vD}}$, even if $\Pr^\star$ is constant. An extended van Driest transformation for the mean temperature profile $\overline{\theta}^\star = \int_0^{\overline{\theta}^{\mathrm{vD}}} [1 + (y/\mathrm{Re}_\tau^\star) d\mathrm{Re}_\tau^\star/dy] d\overline{\theta}^{\mathrm{vD}}$ is derived, which is able to collapse cases with varying $\mathrm{Re}_\tau^\star$ and constant $\Pr^\star$. For cases with varying $\Pr^\star$ profiles, the thickness of the conduction-dominated region changes. The turbulent diffusivity, however, shows a good collapse in the inner layer (except in regions with $y^\star < 10$) for all cases, irrespective of $\mathrm{Re}_\tau^\star$ and $\Pr^\star$ profiles. The modulation in turbulent diffusivity in regions with $y^\star < 10$ occurs for cases with gradients in $\mathrm{Re}_\tau^\star$ and is associated with modulations in turbulence. The modulation is highlighted using the joint probability distribution functions of velocity and temperature fluctuations. However, for the present cases the influence of this turbulence modulation on $\overline{\theta}^\star$ is negligible and its shift in the overlap layer is only caused by $\Pr^\star$ variations. The $\overline{\theta}^\star$ transformation is analogous to the $\overline{u}^\star$ transformation and follows from the strong analogy between momentum transfer and scalar transport, as seen with the turbulent Prandtl number, which varies slightly around unity in the inner layer. Higher order statistics also show quasisimilarity for cases with similar $\mathrm{Re}_\tau^\star$ and $\Pr^\star$ distributions.

The present work focuses on a calorifically perfect fluid at the low-Mach-number limit and heated with a uniform heat source. It will be interesting to see the behavior of scalar statistics in supersonic cases with adiabatic, heated, or cooled walls, where the heat source is due to viscous heating and coupled to the momentum equation, as well as in low-Mach-number cases with different thermal boundary conditions and calorifically imperfect fluids, such as those at supercritical pressure.

ACKNOWLEDGMENTS

---

[1] J. Kim and P. Moin, Transport of passive scalars in a turbulent channel flow, in *Turbulent Shear Flows 6* (Springer, Berlin, 1989), pp. 85–96.

[2] H. Kawamura, K. Ohsaka, H. Abe, and K. Yamamoto, DNS of turbulent heat transfer in channel flow with low to medium-high Prandtl number fluid, Int. J. Heat Fluid Flow **19**, 482 (1998).

[3] F. Schwertfirm and M. Manhart, DNS of passive scalar transport in turbulent channel flow at high Schmidt numbers, Int. J. Heat Fluid Flow **28**, 1204 (2007).

[4] H. Kawamura, H. Abe, and Y. Matsuo, DNS of turbulent heat transfer in channel flow with respect to Reynolds and Prandtl number effects, Int. J. Heat Fluid Flow **20**, 196 (1999).

[5] S. Pirozzoli, M. Bernardini, and P. Orlandi, Passive scalars in turbulent channel flow at high Reynolds number, J. Fluid Mech. **788**, 614 (2016).

[6] J. Y. Yoo, The turbulent flows of supercritical fluids with heat transfer, Annu. Rev. Fluid Mech. **45**, 495 (2013).

[7] H. Nemati, A. Patel, B. J. Boersma, and R. Pecnik, Mean statistics of a heated turbulent pipe flow at supercritical pressure, Int. J. Heat Mass Transfer **83**, 741 (2015).

[8] J. W. R. Peeters, R. Pecnik, M. Rohde, T. H. J. J. van der Hagen, and B. J. Boersma, Turbulence attenuation in simultaneously heated and cooled annular flows at supercritical pressure, J. Fluid Mech. **799**, 505 (2016).

[9] G. N. Coleman, J. Kim, and R. D. Moser, A numerical study of turbulent supersonic isothermal-wall channel flow, J. Fluid Mech. **305**, 159 (1995).

[10] R. Lechner, J. Sesterhenn, and R. Friedrich, Turbulent supersonic channel flow, J. Turbulence **2**, N1 (2001).

[11] H. Foysi, S. Sarkar, and R. Friedrich, Compressibility effects and turbulence scalings in supersonic channel flow, J. Fluid Mech. **509**, 207 (2004).

[12] D. Modesti and S. Pirozzoli, Reynolds and Mach number effects in compressible turbulent channel flow, Int. J. Heat Fluid Flow **59**, 33 (2016).

[13] F. Zonta, C. Marchioli, and A. Soldati, Modulation of turbulence in forced convection by temperature-dependent viscosity, J. Fluid Mech. **697**, 150 (2012).

[14] F. Nicoud and T. Poinsot, DNS of a channel flow with variable properties, in *International Symposium on Turbulence and Shear Flow Phenomena (TSFP-1)* (Begell House, Santa Barbara, California, 1999), p. 697.

[15] A. Patel, J. W. R. Peeters, B. J. Boersma, and R. Pecnik, Semi-local scaling and turbulence modulation in variable property turbulent channel flows, Phys. Fluids **27**, 095101 (2015).

[16] A. Patel, B. J. Boersma, and R. Pecnik, The influence of near-wall density and viscosity gradients on turbulence in channel flows, J. Fluid Mech. **809**, 793 (2016).

[17] J. Lee, S. Y. Jung, H. J. Sung, and T. A. Zaki, Turbulent thermal boundary layers with temperature-dependent viscosity, Int. J. Heat Fluid Flow **49**, 43 (2014).

[18] B. A. Kader, Temperature and concentration profiles in fully turbulent boundary layers, Int. J. Heat Mass Transfer **24**, 1541 (1981).

[19] H. Nemati, A. Patel, B. J. Boersma, and R. Pecnik, The effect of thermal boundary conditions on forced convection heat transfer to fluids at supercritical pressure, J. Fluid Mech. **800**, 531 (2016).

[20] W. M. Kays and M. E. Crawford, *Convective Heat and Mass Transfer* (McGraw-Hill, New York, 1993).

[21] H. Kong, H. Choi, and J. S. Lee, Direct numerical simulation of turbulent thermal boundary layers, Phys. Fluids **12**, 2555 (2000).

[22] Q. Li, P. Schlatter, L. Brandt, and D. S. Henningson, DNS of a spatially developing turbulent boundary layer with passive scalar transport, Int. J. Heat Fluid Flow **30**, 916 (2009).

[23] P. G. Huang, G. N. Coleman, and P. Bradshaw, Compressible turbulent channel flows: DNS results and modelling, J. Fluid Mech. **305**, 185 (1995).

[24] A. Trettel and J. Larsson, Mean velocity scaling for compressible wall turbulence with heat transfer, Phys. Fluids **28**, 026102 (2016).

[25] A. Majda and J. Sethian, The derivation and numerical solution of the equations for zero Mach number combustion, Combust. Sci. Technol. **42**, 185 (1985).

[26] S. K. Lele, Compact finite difference schemes with spectral-like resolution, J. Comput. Phys. **103**, 16 (1992).

[27] B. J. Boersma, A 6th-order staggered compact finite difference method for the incompressible Navier-Stokes and scalar transport equations, J. Comput. Phys. **230**, 4940 (2011).

[28] P. A. McMurtry, W. H. Jou, J. Riley, and R. W. Metcalfe, Direct numerical simulations of a reacting mixing layer with chemical heat release, AIAA J. **24**, 962 (1986).

[29] J. Lee, S. Y. Jung, H. J. Sung, and T. A. Zaki, Effect of wall heating on turbulent boundary layers with temperature-dependent viscosity, J. Fluid Mech. **726**, 196 (2013).

[30] Y. Morinishi, S. Tamano, and K. Nakabayashi, Direct numerical simulation of compressible turbulent channel flow between adiabatic and isothermal walls, J. Fluid Mech. **502**, 273 (2004).